Ligand-free ZnS nanoparticles: as easy and green as it gets - ESI

Nicola Dengo[a], Andrea Faresin[a], Tommaso Carofiglio[a], Michele Maggini[a]*, Longfei Wu[b], Jan P. Hofmann[b], Emiel J. M. Hensen[b], Paolo Dolcet[a,c], and Silvia Gross[a]*

[a]Dipartimento di Scienze Chimiche, Università degli Studi di Padova and INSTM UdR, via Marzolo, 1, 35131, Padova, Italy. E-mail silvia.gross@unipd.it, michele.maggini@unipd.it
[b]Laboratory for Inorganic Materials and Catalysis, Department of Chemical Engineering and Chemistry, Eindhoven University of Technology, P.O. Box 513, 5600 MB Eindhoven, The Netherlands.
[c]Karlsruher Institut für Technologie (KIT), Institut für Technische Chemie und Polymerchemie (ITCP), Engesserstr. 20, 76131 Karlsruhe, Germany.

Experimental Section

Chemicals. Zinc nitrate hexahydrate ($Zn(NO_3)_2 \cdot 6H_2O$, ≥99.0%), sodium sulfide nonahydrate ($Na_2S \cdot 9H_2O$, ≥99.99%) were purchased by Sigma-Aldrich. All chemicals were used without further purification. MilliQ-quality water was used for both synthesis and purification of the materials.

Batch Route. In the batch synthetic approach, 25 ml of a 0.2 M Na_2S solution was kept vigorously stirred in an ice bath to ensure a stable reaction temperature over time, while 25 ml of a 0.1 M $Zn(NO_3)_2$ solution was added dropwise (roughly one drop every two seconds). The product was isolated by centrifugation (5 min, 10 000 rpm), then it was washed by adding fresh water and sonicating the suspension for 15 min prior to isolate the product again by centrifugation (5 - 15 min, 12 500 rpm). This washing cycle was repeated four times. The clean product was dried in vacuum at room temperature using a desiccator, then grinded and stored in common Eppendorf vials.

Microfluidics Route (MF). In the microfluidic approach, the setup depicted in Figure S1 was employed. The Zn and S precursors solutions were pumped using two reciprocating syringe pumps (Asia Syringe Pump, Syrris) operated at 1.2 ml/min. 0.63 mm PTFE tubing and a stainless-steel T-junction mixer were used to realize the flow setup. The solutions were fed asymmetrically to the mixer, having the zinc solution connected in the position aligned with the mixer outlet and the sulfur solution connected at 90° with respect to both the zinc precursor and the outlet positions (cross-flow T-junction). The product was collected in an ice bath-cooled stirred vessel prefilled with approx. 20 ml of water. Once the targeted amount of product was obtained, the setup was flowed with water before the pumps were shuttled down, to prevent the occlusion of the mixer. The obtained slurry was kept stirred for approx. 1h and then let settle down. Once the product was settled, the clear solution above was carefully removed and the product was recovered washing the flask with fresh water. The product was isolated though centrifugation (5 min, 10 000 rpm), then it was washed by adding fresh water and sonicating the suspension for 15 min prior to isolate the product again by centrifugation (5 - 15 min, 12 500 rpm). This washing cycle was repeated four times. The clean product was dried in vacuum at room temperature using a desiccator, then grinded and stored in common Eppendorf vials.
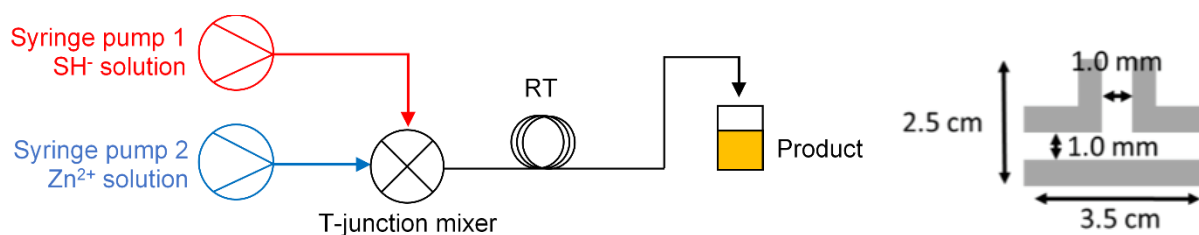
Figure S1 (a) Microfluidic set-up for the synthesis of ZnS colloidal suspensions. (b) Schematic representation of the employed T-junction mixer.

XPS Spectroscopy. Powder samples were investigated by XPS with a Perkin–Elmer φ 5600ci instrument using Al-Kα radiation (1486.6 eV), operating at 350 W. The working pressure was less than $5·10^{-8}$ Pa. The calibration was based on the binding energy (BE) of the Au $4f_{7/2}$ line at 83.9 eV with respect to the Fermi level. The standard deviation for the BE values was 0.15 eV. Reported BEs were corrected for charging effects and the BE value of 284.6 eV was assigned to the C1s line of carbon. Survey scans were obtained in the 0–1350 eV range (pass energy 187.5 eV, 1.0 eV step^{-1}, 25 ms step^{-1}). Detailed scans (29.35 eV pass energy, 0.1 eV step^{-1}, 50–150 ms step^{-1}) were recorded for O1s, C1s, Zn2p, ZnLMM, S2p, and S2s. The atomic composition, after a Shirley-type background subtraction[1] was evaluated using sensitivity factors supplied by Perkin–Elmer. Peak assignment was carried out according to literature data. Peak fittings were performed using the software XPSPeak 4.1 accounting for the spin-orbit splitting of the signals.

XRD Diffraction. The XRD patterns on the ZnS nanostructures were collected with a Bruker D8 Advance Diffractometer equipped with a Göbel mirror by using the Cu-Kα radiation. The angular accuracy was 0.0010° and the angular resolution was better than 0.01°. All the experimental data were analyzed by using the Material Analysis Using Diffraction (MAUD) software package,[2] to deduce quantitative crystallographic and microstructural information by using the Rietveld refinement method. The effect of size and size distribution on the patterns was accounted together with the presence of size-dependent strain by using the model developed by Popa and Balzar.[3] The presence of microstrain was considered for the microfluidic samples as surface-induced strain was expected to be relevant due the small size of the NPs.[4] The presence of planar defects was accounted using the Warren model.[5] Since many effects contributes simultaneously to the broadening of the reflections, making difficult to reliably distinguish between contribution arising from different crystallographic features, the fitting procedure was aided from the fitted size distributions retrieved by the TEM analysis.

TEM Microscopy. TEM micrographs where obtained with a FEI Tecnai G12 microscope operating at 100 kV, equipped with an OSIS Veleta camera. Samples were prepared by suspending the dried powders in ethanol through sonication and then deposited on 300 mesh lacey carbon coated copper grids. Particles were manually segmented and measured using the ImageJ package.[6] The obtained distributions were fitted using the log-normal distribution.

Raman Spectroscopy. Raman spectra were collected using a Thermo Scientific DXR Raman micro-spectrometer equipped with a 532 nm laser and using a 10x LWD. The spectral range was 100 – 3500 cm^{-1}.

Diffuse Reflectance Spectroscopy (DSR). The spectra were measured on a Cary 5E equipped with an interface-diffuse reflectance accessory mirror unit and recorded with a 0.66 nm stepsize. PTFE was utilized as standard reference, and the reflectance spectra were converted using the Kubelka–Munk function: $F(R) = (1 - R)^2 / 2R$. To extrapolate the direct band gap, the Tauc method was applied as $F(R)hv = cost(hv - E_g)^{0.5}$.

Fourier-Transform Infrared Spectroscopy (FTIR). The FTIR spectra were measured with a Nicolet Nexus 870 FTIR equipped with an Attenuated Total Reflectance (ATR) accessory using a diamond ATR crystal. FTIR spectra were acquired in the $4000 - 400$ cm^{-1} range, collecting 512 scans with a spectral resolution of 4 cm^{-1}. The background subtraction was performed interpolating the obtained spectra with a cubic spline function.

Photocatalytic H$_2$ Evolution. All photocatalytic experiments were performed in a home-built air-tight photocatalytic setup in a side-illuminated PEEK cell.[7] A 500 W Hg (Xe) lamp was used as the light source, and the amount of H$_2$ produced during the experiments was detected with an online GC-TCD (ShinCarbon column) with N$_2$ as the carrier gas. Therefore, the amount of produced hydrogen was determined as a function of time to compare the photocatalytic activities among samples. In a typical test, 10 mg photocatalyst was dispersed under sonication in 50 mL sacrificial agents' solution (0.25 M Na$_2$S and 0.35 M Na$_2$SO$_3$) and transferred into the PEEK cell to generate a photocatalyst loading of 0.2 g/l. Before each test, air in the system was removed by evacuation three times. Then the activity measurements were carried out under constant stirring with automated sampling of the gaseous products with 12 min intervals. The temperature of the solution was maintained at 20°C by constant temperature circulating water.

XPS Spectroscopy

The adventitious C1s peak was used to correct the XPS spectra for charging effects by assigning the peak value to 284.6 eV.[8] The semi-quantitative analysis carried out on the $Zn2p_{3/2}$ and S2p peaks resulted in a Zn:S atomic ratio of 1:0.9 for the batch sample, whereas a 1:0.7 ratio was obtained for the MF1 sample. The $Zn2p_{3/2}$ peaks were found at 1021.7 and 1021.8 eV for the batch and MF1 samples respectively, as typical for Zn^{2+}.[9–11] In the S2p region only one peak located at 161.5 and 161.6 eV for the batch and the MF1 samples, respectively, was retrieved. This peak is consistent with the presence of only the S^{2-} oxidation state, with no visible contributions from higher oxidation states (i.e. sulfites or sulfates normally found around 169 eV).[12] Moreover, in the O1s region, only one peak at 531.7 eV was found, which was attributed to adventitious contamination. Indeed, analogous signals belonging to Zn-O moieties would be peaked at about 530 eV and were not observed in these samples.[13] Overall, despite the variation with respect to the nominal ZnS stoichiometry, the material was obtained pure and free of detectable oxidation.
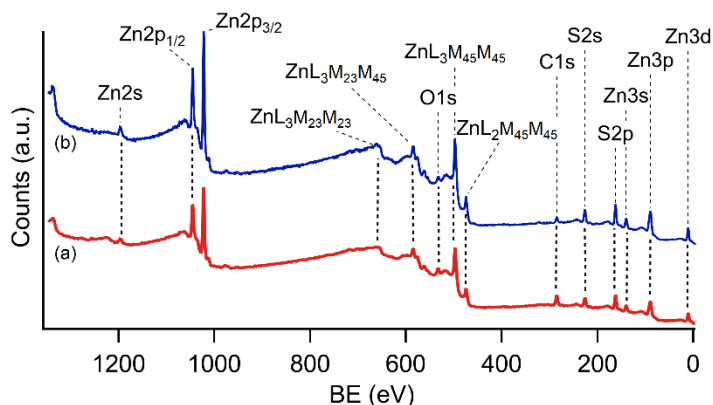
Figure S2 XPS survey spectra of the batch sample (a) and sample MF1 (b).

Table S1 Retrieved peaks position in the XPS spectra of Batch and MF1 samples

Peak	Batch (ev)	MF1 (ev)	References[9] (ev)
Zn2s	1196.6	1196.6	1196
Znp3/2	1021.7	1021.8	1021.7 - 1022.0
Zn3s	139.8	140.2	141.5 - 139.9
Zn3p	86.6	89.4	88.4
Zn3d	10.2	10.6	9.8 - 10.7
S2s	226.2	226.6	225.6 - 226.3
S2p	161.5	161.6	161.9 - 162.2

TEM Microscopy
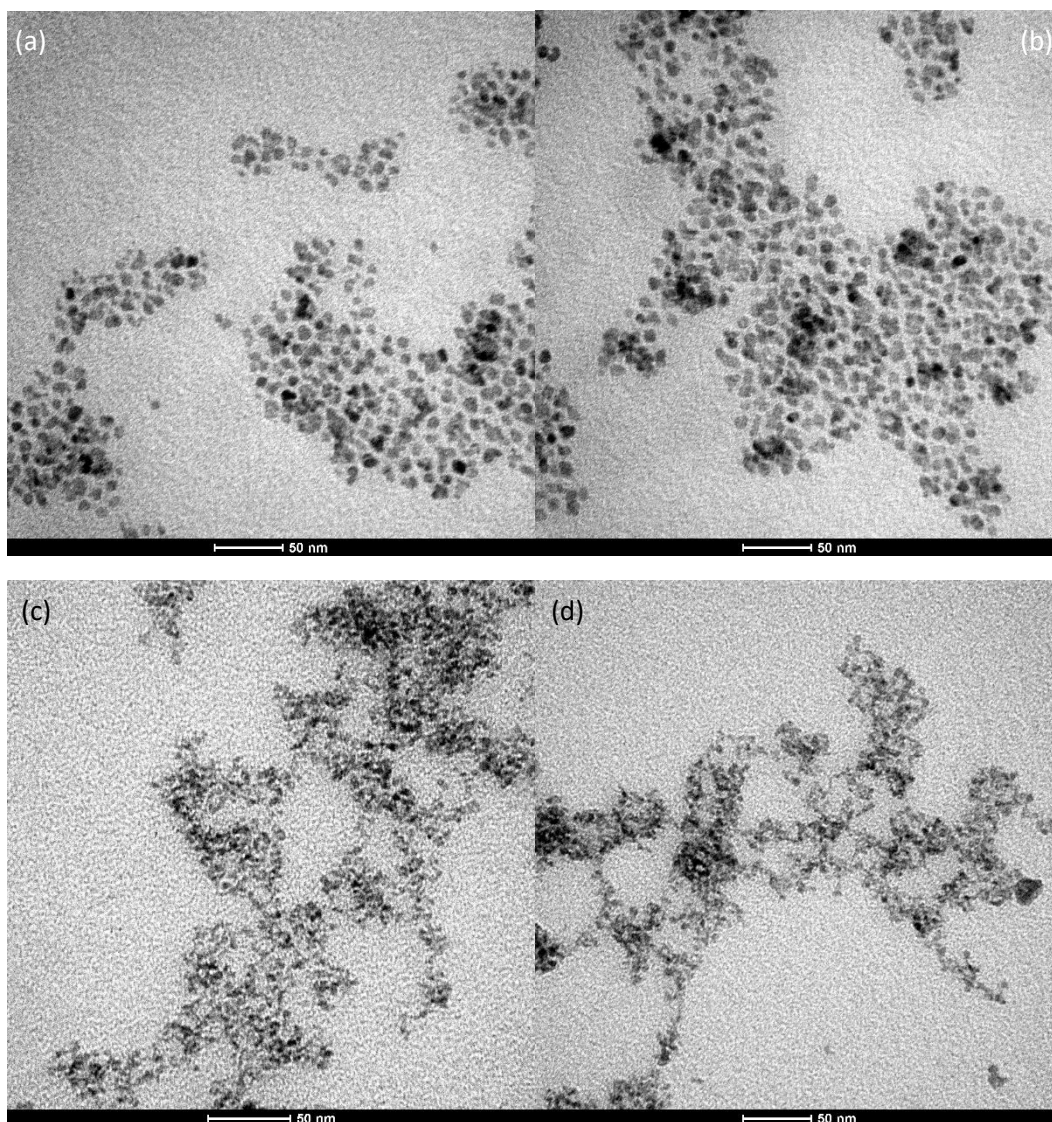
Figure S3 TEM micrographs of the Batch sample (a, b) and sample MF1 (c, d). (continues)
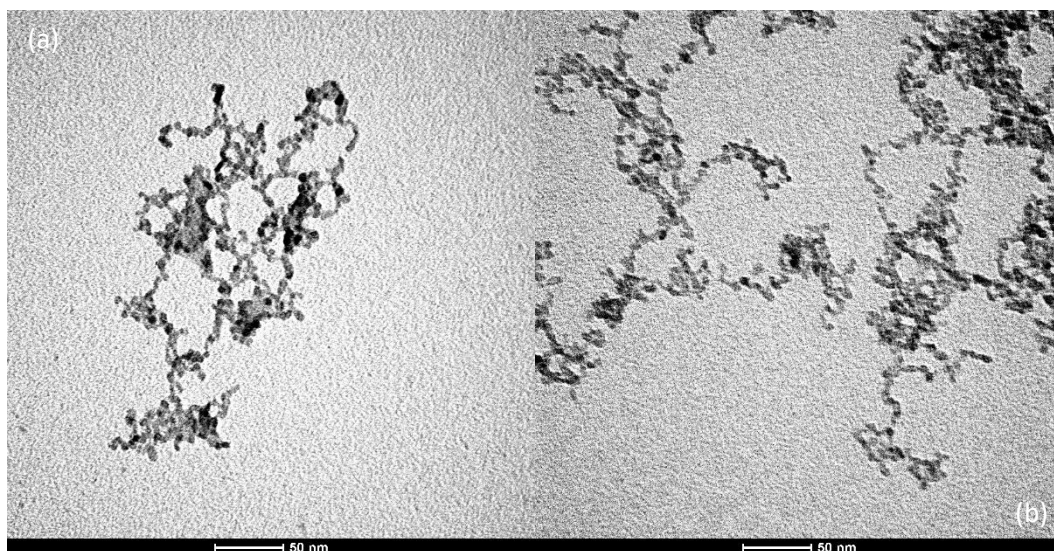
Figure S4 TEM micrographs of the sample MF2 (e, f).

Table S2 Size distribution descriptors obtained from TEM population of sampled particles and from TEM distributions fitting.

	MF1		MF2		Batch	
	TEM	fit	TEM	fit	TEM	fit
$D_{1,0}$ (nm)	4.8	5.3	6.6	7.1	7.8	8.4
Std. dev. (nm)	0.8 (17%)	1.0 (19%)	1.0 (20%)	1.2 (14%)	1.2 (16%)	1.2 (14%)
$D_{3,2}$ (nm)	5.0	5.7	6.9	7.5	8.1	8.7
$D_{4,3}$ (nm)	5.1	5.9	7.0	7.6	8.3	8.9
Skewness	0.4	0.6	0.5	0.4	0.1	0.4
Kurtosis	-0.8	0.6	-0.5	0.4	0.5	0.3

XRD Diffraction
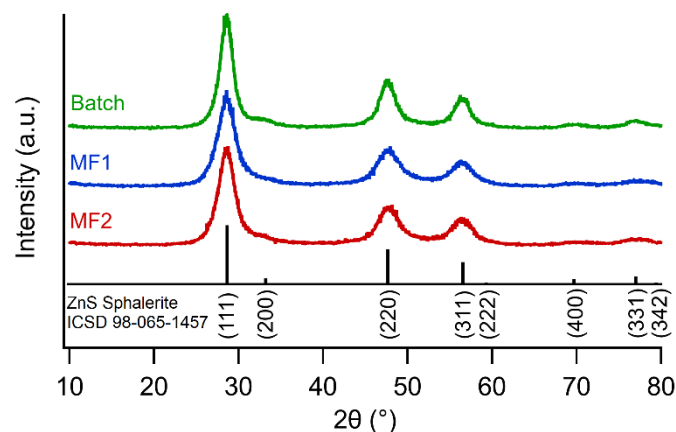
Figure S5 XRD diffractograms of the samples displayed with a comparison to the position and the relative intensity of the bulk ZnS sphalerite reflections (stick plot) from ICSD No. 98-065-1457.

Table S3 Comparison between the size distribution descriptors obtained from the log-normal fits of the experimental size distribution obtained by TEM analysis and the distribution obtained by fitting the XRD patterns of the samples.

	MF1		MF2		Batch	
	TEM-fit	Refined	TEM-fit	Refined	TEM-fit	Refined
$D_{1,0}$ (nm)[a]	5.3	6.3	7.1	8.1	8.4	8.1
Std. dev.	1.0 (19%)	2.6 (41%)	1.1 (15%)	1.6 (20%)	1.2 (14%)	0.7 (9%)
$D_{3,2}$ (nm)[a]	5.7	8.6	7.5	8.7	8.7	8.2
$D_{4,3}$ (nm)[a]	5.9	10	7.6	9.1	8.9	8.2
Skewness	0.6	1.3	0.4	0.6	0.4	0.3
Kurtosis	0.6	3.1	0.4	0.7	0.3	0.1
GoF[b]		1.6		1.7		1.6
SF probability[c]		0.09		0.08		0.04

[a]Average diameter values are referred as $D_{n,m}$, being the ratio of the nth over the mth moments about zero of the considered distribution. $D_{1,0}$ = numeric average; $D_{2,3}$ = surface-weighted average, $D_{4,3}$ = volume-weighted average. [b]GoF = goodness of fit. [c]SF = stacking faults.

Raman Spectroscopy

Raman analysis was employed to check the structural and compositional features of the samples. The Raman spectra of the Batch and MF1 samples are reported and compared with a reference spectrum obtained from cubic ZnS NPs having an average size of 21 nm (Figure S6a). In general, the expected first and second order Raman spectra of sphalerite ZnS was observed, as reported in Table S4. Additionally, a sharp component at around 1000 cm^{-1} was also retrieved, which was attributed to the Raman-active asymmetric stretching mode of surface sulfates.[14] Since the relative intensity of this signal was observed to increase during the analyses, the formation of sulfates was likely related to light- or heat-induced oxidation of the material. Indeed, ZnS was found to be susceptible to oxidation even after exposure to moderately high temperatures.[13]

By comparing the spectral pattern of the cubic ZnS obtained for the samples with the 21 nm NPs reference, some differences were evidenced. The profile of the LO peak was noticeably asymmetrically broadened toward smaller wavenumbers, as visible in Figure S6b. This effect was commonly found in small NPs and was attributed to the quantum confinement of phonons[15], and is generally evident in the whole profile, as in the Batch and the MF1 samples the spectral features were less sharp and resolved. Another relevant variation was the increase of the relative intensity of the TO mode, which was weak in the reference spectra but got more intense in the Batch sample, while in sample MF1 it became even more intense than the LO peak. No information was retrieved in the available literature on this effect. Since this variation was likely to reflect the structural features of the samples, it is possible to hypothesize that this effect might be related to the NPs size or to the presence of defects in the crystal structure, as also suggested by XPS and DSR analyses.
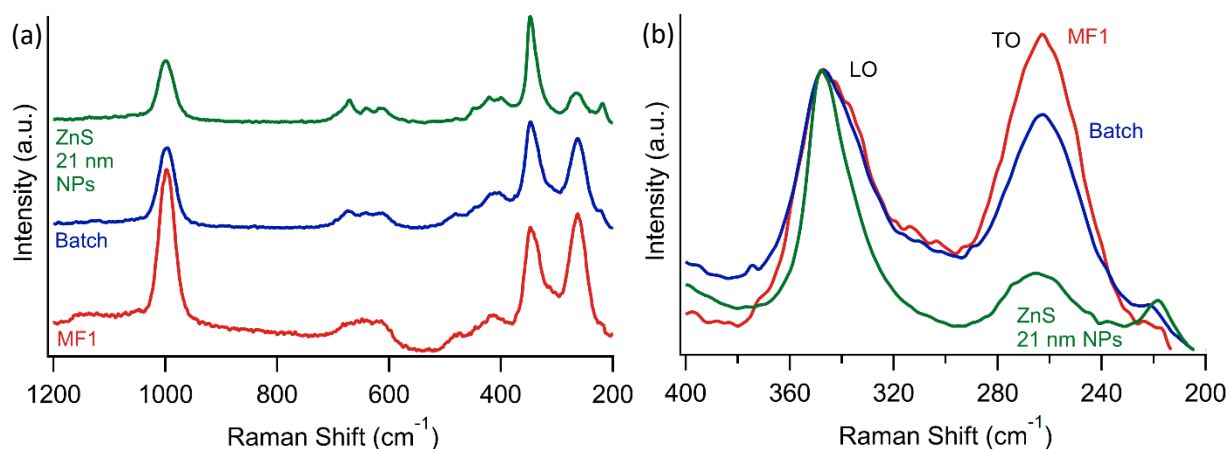
Figure S6 (a) Raman spectrum of sample MF1 compared with Raman spectra of the Batch sample and with a reference sample of ZnS NPs of 21 nm. (b) Detail of the broadening effects on the LO mode and on the increased relative intensity of the TO mode. Intensities were normalized on the LO phonon.

Table S4 Peaks attribution of the Raman spectra of ZnS1 and ZnS2 samples compared with reference sample (ZnS 21 nm NPs) and values from the literature.

Peak	Batch (cm^{-1})	MF1 (cm^{-1})	ZnS 21 nm (cm^{-1})	References[16,17] (cm^{-1})
TO	263	263	265	278, 275
LO	347	347	348	354, 350
2(0) on W	220	-	218	218, 219
TO+LA	412[a]	412[a]	399	401, 386
TO+LA	412[a]	412[a]	421	424, 422
2(0) on W	447	446	449	458, 448
2(TO)	612	612[b]	612	618, 612
2(TO)	641	641[b]	641	643, 636
2(TO)	671	671[b]	671	677, 665

[a]The two TO+LA components appeared overlapped in a single broad component. [b]Estimated position.

Diffuse Reflectance Spectroscopy (DSR)

The optical properties of the powders were assessed using Diffuse Reflectance Spectroscopy (DSR). The obtained spectra (Figure S7a) showed the typical absorption edge of ZnS at 340 nm. The presence of weak absorption features at the base of the absorption edge was also evident for samples MF1 and MF2. These features are likely related to the presence of point defects like S vacancies in the crystal structure of the ZnS NPs, as also suggested by the XPS analysis.[18] This result is coherent with the general increased presence of defects in the crystal structure of the microfluidic samples in comparison with the Batch sample. The greater prominence of the absorption feature in sample MF1 suggests that a larger amount of defects was formed in comparison with sample MF2.

The Tauc analysis was applied to the DSR spectra converted with the Kubelka-Munk function (Figure S7b). Similar direct band gap values were obtained for all the samples: 3.30 eV for the batch and MF2 samples and 3.25 eV for sample MF1 The retrieved values are close to the reference value of 3.66 eV.[19] The slight redshift of the bandgap value was already reported and attributed to the influence on the Tauc plot of the tailing produced by the defect states at lower energy values.[20] The presence quantum confinement effects and the consequent blueshift of the bandgap was not expected, as the size of the NPs (form 7.8 to 4.8 nm) is considerably bigger than the exciton Bohr radius (2.5 nm).[21]
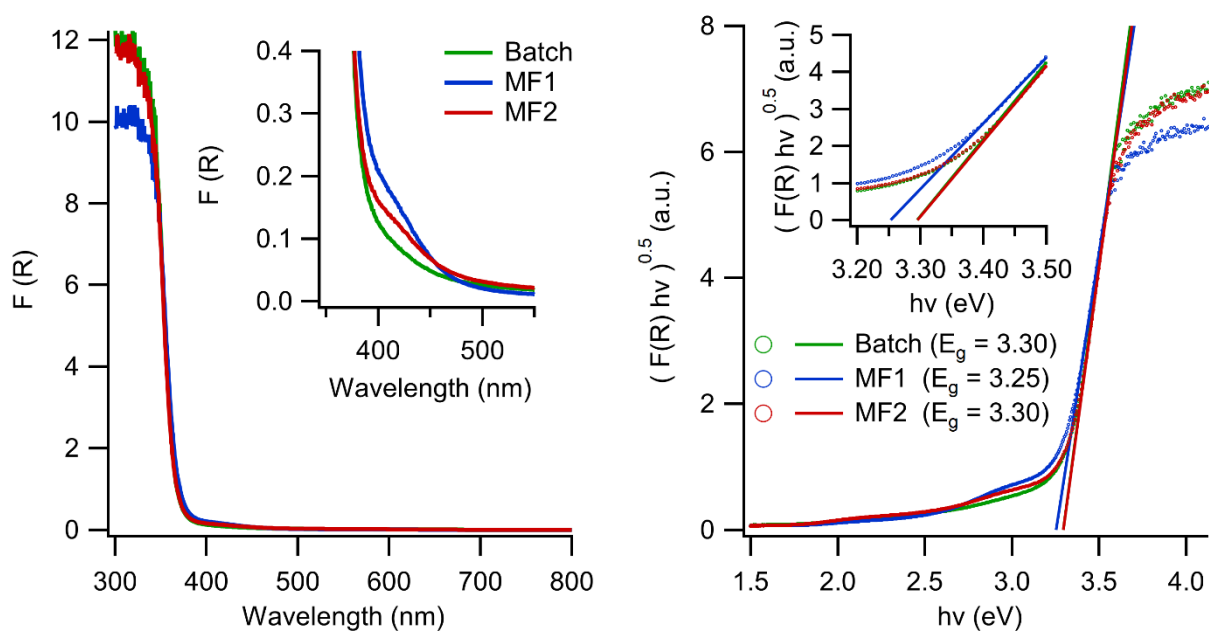
Figure S7 (a) DSR spectra of the samples. (b) Tauc plot for the extrapolation of the direct bandgap values of the samples.

Fourier-Transform Infrared Spectroscopy (FTIR)

The surface analysis of the samples was complemented with FTIR spectroscopy, to detect the presence of functional groups or adsorbed moieties. The obtained spectra for the three samples were almost identical (Figure S8), and the retrieved features were analogous to ZnS NPs obtained using hydrothermal routes.[12] The most prevalent feature is the presence of the broad HOH stretching (around 3300 cm^{-1}) and HOH bending (1628 cm^{-1}), attributed to H_2O molecules adsorbed on the NPs surface.[12] The two peaks at 1005 cm^{-1} and 1119 cm^{-1} are typical of surface sulfates moieties. The first corresponds to a non-degenerate (single) symmetric stretching mode, while the second results from the overlap of three non-degenerate (single) asymmetric stretching modes.[12] Since no sulfates were evident at the XPS analysis, the concentration of such species must lie below the XPS sensitivity level (approximatively 0.1% atomic of the probed sample) and can be referred as traces. The presence of the XPS peaks for the sulfates (i.e. the S2p component for S in 6+ oxidation state) along with more intense FTIR peaks were reported in the case of ZnS NPs having relevant surface oxidation.[13] The weak shoulder centered around 1421 cm^{-1} can be attributed to adsorbed carbonates, possibly formed from the interaction of atmospheric CO_2 with the adsorbed H_2O.[12] The peak at 634 cm^{-1} is not related to functional groups or adsorbed moieties, but can instead be attributed to the transversal optical mode TO (phonon) at the X critical point of the Brillouin zone of ZnS sphalerite.[16] Overall, the analysis confirmed that the obtained ZnS NPs were free of relevant surface oxidation product, despite the synthesis was simply carried out in water and in air-exposed conditions.
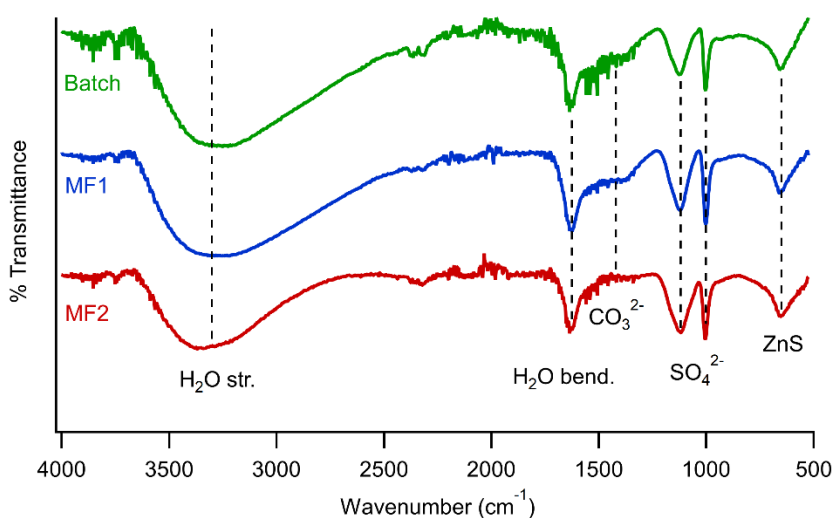
Figure S8 FTIR spectra of the samples.

Acknowledgements

References

1   D. A. Shirley, *Phys. Rev. B*, 1972, **5**, 4709–4714.

2   L. Lutterotti, *Nucl. Instruments Methods Phys. Res. Sect. B*, 2010, **268**, 334–340.

3   D. Balzar and N. C. Popa, in *Diffraction Analysis of the Microstructure of Materials*, 2004, pp. 125–145.

4   B. Gilbert, *Science (80-.).*, 2004, **305**, 651–654.

5   B. E. Warren, *J. Appl. Phys.*, 1961, **32**, 2428–2431.

6   C. A. Schneider, W. S. Rasband and K. W. Eliceiri, *Nat. Methods*, 2012, **9**, 671–675.

7   A. Litke, J. P. Hofmann, T. Weber and E. J. M. Hensen, *Inorg. Chem.*, 2015, **54**, 9491–9498.

8   T. L. Barr and S. Seal, *J. Vac. Sci. Technol. A*, 1995, **13**, 1239–1246.

9   NIST X-ray Photoelectron Spectroscopy Database, Version 4.1 (National Institute of Standards and Technology, Gaithersburg, 2012);, http://srdata.nist.gov/xps/.

10   P. Dolcet, C. Maurizio, M. Casarin, L. Pandolfo, S. Gialanella, D. Badocco, P. Pastore, A. Speghini and S. Gross, *Eur. J. Inorg. Chem.*, 2015, **2015**, 706–714.

11   E. Agostinelli, C. Battistoni, D. Fiorani, G. Mattogno and M. Nogues, *J. Phys. Chem. Solids*, 1989, **50**, 269–272.

12   N. Dengo, A. Vittadini, M. M. Natile and S. Gross, *J. Phys. Chem. C*, 2020, **124**, 7777–7789.

13   N. Dengo, A. F. De Fazio, M. Weiss, R. Marschall, P. Dolcet, M. Fanetti and S. Gross, *Inorg. Chem.*, 2018, **57**, 13104–13114.

14   K. Nakamoto, *Infrared and Raman Spectra of Inorganic and Coordination Compounds*, John Wiley & Sons, Inc., Hoboken, NJ, USA, 2008.

15   N. Karar, F. Singh and B. R. Mehta, *J. Appl. Phys.*, 2004, **95**, 656–660.

16   Y. C. Cheng, C. Q. Jin, F. Gao, X. L. Wu, W. Zhong, S. H. Li and P. K. Chu, *J. Appl. Phys.*, 2009, **106**, 123505–123510.

17   W. G. Nilsen, *Phys. Rev.*, 1969, **182**, 838–850.

18   G. Wang, B. Huang, Z. Li, Z. Lou, Z. Wang, Y. Dai and M.-H. Whangbo, *Sci. Rep.*, 2015, **5**, 8544.

19   F. Kurnia and J. N. Hart, *ChemPhysChem*, 2015, **16**, 2397–2402.

20   S. P. Patel, J. C. Pivin, R. Chandra, D. Kanjilal and L. Kumar, *J. Mater. Sci. Mater. Electron.*, 2016, **27**, 5640–5645.

21   Z. Deng, L. Tong, M. Flores, S. Lin, J. X. Cheng, H. Yan and Y. Liu, *J. Am. Chem. Soc.*, 2011, **133**, 5389–5396.